

Strömgren sphere radii for the observed SDSS quasars. This is in contrast to the simplified monolithic model of quasar formation<sup>16,1</sup>, for which the H II region has zero volume at the time when the quasar turns on [ $R(t_{\text{age}} = 0) = 0$ ] and the distribution extends down to  $R_p = 0$ .

To constrain the neutral fraction, we have computed the likelihood of observing  $R_{\text{obs}} = 4.5$  Mpc around SDSS J1030+0524 and  $R_{\text{obs}} = 4.7$  Mpc around SDSS J1148+5251 as a function of  $x_{\text{HI}}$  and  $f_{\text{I}t}$ . The results are plotted in Fig. 2. Figure 2a shows the locus of most likely values (thick line) as well as likelihood contours at 0.1 of the peak value (dashed lines). The fiducial lifetime ( $f_{\text{I}t}$ ) favours  $x_{\text{HI}} \approx 1$ , while with  $f_{\text{I}t} \ll 1$  the distributions for  $R_p$  lie substantially below the observed value of 4.5 Mpc, making smaller values of  $x_{\text{HI}}$  more likely. Extrapolation of the most likely contour for the Elvis *et al.*<sup>19</sup> template yields  $f_{\text{I}t} \approx 2x_{\text{HI}}$ . This implies that  $x_{\text{HI}} \approx 10^{-3}$  would require a lifetime as short as  $2 \times 10^4$  years, which is ruled out by the variability properties of quasars in SDSS<sup>26</sup>. The a posteriori probability distributions for  $x_{\text{HI}}$  given  $f_{\text{I}t}$  are plotted in Fig. 2b and robustly yield the constraint  $x_{\text{HI}} \geq 0.01$ . For  $f_{\text{I}t} \geq 0.3$ , we find  $x_{\text{HI}} \geq 0.1$  and  $x_{\text{HI}} \geq 0.4$  at the 90% level for the Elvis *et al.*<sup>19</sup> and Telfer *et al.*<sup>18</sup> spectra, respectively. The fiducial model with  $f_{\text{I}t} = 1$  yields corresponding constraints of  $x_{\text{HI}} \geq 0.3$  and  $x_{\text{HI}} \geq 0.6$ .

The inference of a large neutral fraction at  $z \approx 6.3$  presents a challenge to theories of cosmological reionization when combined with the large optical depth<sup>3</sup> to electron scattering after cosmological recombination,  $\tau_{\text{es}} = 0.17 \pm 0.04$ . Consider a toy model in which the Universe was partially reionized at a high redshift  $z_{\text{reion,I}}$ , leaving a neutral fraction  $x_{\text{HI}}$  until complete reionization was reached at  $z_{\text{reion,II}} \approx 6.25$ . The optical depth is then  $\tau_{\text{es}} = 0.04 + 0.002(1 - x_{\text{HI}})[(1 + z_{\text{reion,I}})^{3/2} - 19.5]$ . If the IGM ionization fraction increased monotonically, then given  $\tau_{\text{es}} > 0.13$ , the Universe needed to be reionized earlier than  $z_{\text{reion,I}} \approx 18$  or  $z_{\text{reion,I}} \approx 24$ , assuming the Elvis *et al.*<sup>19</sup> and Telfer *et al.*<sup>18</sup> spectra, respectively. If  $\tau_{\text{es}} = 0.17$  and  $x_{\text{HI}} > 0.7$ , as implied by the Telfer *et al.*<sup>18</sup> spectrum, then a monotonic reionization history requires significant reionization at an implausibly high redshift ( $z \geq 30$ ). In this case, a more plausible alternative is a non-monotonic history with an early reionization peak, possibly due to the formation of massive population-III stars<sup>27,28</sup>. □

Received 14 October 2003; accepted 15 January 2004; doi:10.1038/nature02336.

1. White, R. L., Becker, R. H., Fan, X. & Strauss, M. A. Probing the ionization state of the universe at  $z > 6$ . *Astron. J.* **126**, 1–14 (2003).
2. Fan, X. *et al.* Evolution of the ionizing background and the epoch of reionization from the spectra of  $z \sim 6$  quasars. *Astron. J.* **123**, 1247–1257 (2002).
3. Kogut, A. *et al.* First-year Wilkinson microwave anisotropy probe (WMAP) observations: temperature-polarization correlation. *Astron. J. Suppl.* **148**, 161–173 (2003).
4. Hu, E. M. *et al.* A redshift  $z = 6.56$  galaxy behind the cluster Abel 370. *Astrophys. J.* **568**, L75–L79 (2002).
5. Haiman, Z. The detectability of high-redshift Ly $\alpha$  emission lines prior to the reionization of the universe. *Astrophys. J.* **576**, L1–L4 (2002).
6. Willott, C. J., McLure, R. J. & Jarvis, M. J. A  $3 \times 10^9 M_{\odot}$  black hole in the quasar SDSS J1148+5251 at  $z = 6.41$ . *Astrophys. J.* **587**, L15–L18 (2003).
7. Walter, F. *et al.* Molecular gas in the host galaxy of a quasar at redshift  $z = 6.42$ . *Nature* **424**, 406–408 (2003).
8. Richards, G. T. *et al.* Broad emission-line shifts in quasars: an orientation measure for radio-quiet quasars? *Astron. J. Suppl.* **124**, 1–17 (2002).
9. Barkana, R. & Loeb, A. In the beginning: the first sources of light and the reionization of the universe. *Phys. Rep.* **349**, 125–238 (2001).
10. Gunn, J. E. & Peterson, B. A. On the density of neutral hydrogen in intergalactic space. *Astrophys. J.* **142**, 1633–1641 (1965).
11. Pentericci, L. *et al.* VLT optical and near-infrared observations of the  $z = 6.28$  quasar SDSS J1030+0524. *Astron. J.* **123**, 2151–2158 (2002).
12. Martini, P. QSO lifetimes. Preprint at (<http://arXiv.org/astro-ph/0304009>) (2003).
13. Miralda-Escude, J., Haehnelt, M. & Rees, M. Reionization of the inhomogeneous universe. *Astrophys. J.* **530**, 1–16 (2000).
14. Barkana, R. & Loeb, A. GRBs versus Quasars: Lyman- $\alpha$  signatures of reionization versus cosmological inflall. *Astrophys. J.* (in the press); preprint at (<http://arXiv.org/astro-ph/0305470>) (2003).
15. Shapiro, P. R. & Giroux, M. L. Cosmological, H II regions and the photoionization of the intergalactic medium. *Astrophys. J.* **321**, L107–L112 (1987).
16. Cen, R. & Haiman, Z. Quasar Stromgren spheres before cosmological reionization. *Astrophys. J.* **542**, L74–L78 (2000).
17. Madau, P. & Rees, M. J. The earliest luminous sources and the damping wing of the Gunn-Peterson trough. *Astrophys. J.* **542**, L69–L73 (2000).

18. Telfer, R. C., Zheng, W., Kriss, G. A. & Davidsen, A. F. The rest-frame extreme-ultraviolet spectral properties of quasi-stellar objects. *Astron. J.* **565**, 773–785 (2002).
19. Elvis, M. *et al.* Atlas of quasar energy distributions. *Astron. J. Suppl.* **95**, 1–68 (1994).
20. Shields, G. A. *et al.* The black hole-bulge relationship in quasars. *Astrophys. J.* **583**, 124–133 (2003).
21. Ferrarese, L. Beyond the Bulge: a fundamental relationship between supermassive black holes and dark matter halos. *Astrophys. J.* **587**, 90–97 (2001).
22. Volonteri, M., Haardt, F. & Madau, P. The assembly and merging history of supermassive black holes in hierarchical models of galaxy formation. *Astrophys. J.* **582**, 559–573 (2003).
23. Yu, Q. & Tremaine, S. Observational constraints on growth of massive black holes. *Mon. Not. R. Astron. Soc.* **335**, 965–976 (2002).
24. Martini, P. & Weinberg, D. H. Quasar clustering and the lifetime of quasars. *Astrophys. J.* **547**, 12–26 (2001).
25. Jakobsen, P., Jansen, R. A., Wagner, S. & Reimers, D. Caught in the act: a helium-reionizing quasar near the line of sight to Q0302003. *Astron. Astrophys.* **397**, 891–898 (2003).
26. Martini, P. & Schneider, D. P. Preprint at (<http://arXiv.org/astro-ph/0309650>) (2003).
27. Wyithe, J. S. B. & Loeb, A. Reionization of hydrogen and helium by early stars and quasars. *Astrophys. J.* **586**, 693–708 (2003).
28. Cen, R. The implications of Wilkinson microwave anisotropy probe observations for population III star formation processes. *Astrophys. J.* **591**, L5–L8 (2003).
29. Miralda-Escude, J. Reionization of the intergalactic medium and the damping wing of the Gunn-Peterson trough. *Astrophys. J.* **501**, 15–22 (1998).
30. Spergel, D. N. *et al.* First-year Wilkinson microwave anisotropy probe (WMAP) observations: determination of cosmological parameters. *Astron. J. Suppl.* **148**, 175–194 (2003).

**Acknowledgements** This work was supported in part by grants from ARC, NSF and NASA.

**Competing interests statement** The authors declare that they have no competing financial interests.

**Correspondence** and requests for materials should be addressed to A.L. (aloeb@cfa.harvard.edu).

## Atomic transient recorder

R. Kienberger<sup>1\*</sup>, E. Goulielmakis<sup>1\*</sup>, M. Uiberacker<sup>1\*</sup>, A. Baltuska<sup>1</sup>, V. Yakovlev<sup>2</sup>, F. Bammer<sup>2</sup>, A. Scrinzi<sup>1</sup>, Th. Westerwalbesloh<sup>3</sup>, U. Kleineberg<sup>3</sup>, U. Heinzmann<sup>3</sup>, M. Drescher<sup>3</sup> & F. Krausz<sup>1,4</sup>

<sup>1</sup>Institut für Photonik, Technische Universität Wien, Gusshausstraße 27, A-1040 Wien, Austria

<sup>2</sup>Institut für Spanlose Fertigung und Hochleistungslasertechnik, Technische Universität Wien, Franz-Grillstr. 1, Arsenal Obj. 207, A-1030 Wien, Austria

<sup>3</sup>Fakultät für Physik, Universität Bielefeld, D-33615 Bielefeld, Germany

<sup>4</sup>Max-Planck-Institut für Quantenoptik, Hans-Kopfermann-Straße 1, D-85748 Garching, Germany

\*These authors contributed equally to this work

In Bohr's model of the hydrogen atom, the electron takes about 150 attoseconds ( $1 \text{ as} = 10^{-18} \text{ s}$ ) to orbit around the proton, defining the characteristic timescale for dynamics in the electronic shell of atoms. Recording atomic transients in real time requires excitation and probing on this scale. The recent observation of single sub-femtosecond ( $1 \text{ fs} = 10^{-15} \text{ s}$ ) extreme ultraviolet (XUV) light pulses<sup>1</sup> has stimulated the extension of techniques of femtochemistry<sup>2</sup> into the attosecond regime<sup>3,4</sup>. Here we demonstrate the generation and measurement of single 250-attosecond XUV pulses. We use these pulses to excite atoms, which in turn emit electrons. An intense, waveform-controlled, few cycle laser pulse<sup>5</sup> obtains 'tomographic images' of the time-momentum distribution of the ejected electrons. Tomographic images of primary (photo)electrons yield accurate information of the duration and frequency sweep of the excitation pulse, whereas the same measurements on secondary (Auger) electrons will provide insight into the relaxation dynamics of the electronic shell following excitation. With the current  $\sim 750\text{-nm}$  laser probe and  $\sim 100\text{-eV}$  excitation, our transient recorder is capable of resolving atomic electron dynamics within the Bohr orbit time.

In electron-optical chronoscopy the rapid deflection of a bunch

of photoelectrons maps their temporal profile to a spatial distribution<sup>6,7</sup>. From the electrons' streaked image the temporal structure of the light pulse triggering the photoemission can be inferred with sub-picosecond resolution. The resolution of streak cameras is limited by the spread of the electron transit time owing to the spread of their initial momenta. In this work we report sampling of sub-femtosecond electron emission from atoms by drawing on the same basic concept. The improved time resolution results from several essential modifications of image-tube streak cameras: the oscillating electric field of light is used for affecting the electrons' motion (1), the field is virtually jitter-free (2), and is applied along the direction of electron motion, which implies their acceleration or deceleration instead of their deflection (3), directly at the location and instant of emission (4). Whereas (1) implies 'only' a dramatically enhanced streaking speed, the consequences of (2)–(4) are more profound: (2) allows us to systematically vary the timing of the probing field with an accuracy within the electron bunch length, and because of (3) this capability results in the 'projection' of the initial time–momentum distribution of electron emission into a series of distributions of the electrons' final momentum, while (4) prevents the initial momentum spread from introducing any measurement error. As a result of (2)–(4), the spread of initial electron momenta no longer limits the time resolution. Moreover, a possible temporal variation of this initial momentum spread during the emission can be captured just as can the temporal variation of the emission intensity.

The final momentum distribution of electrons detached from atoms by an impulsive excitation in the presence of an intense,

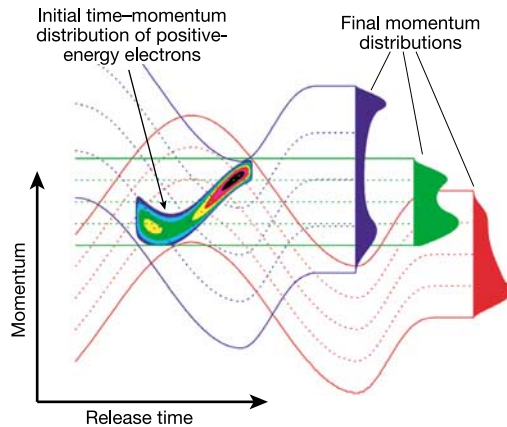


**Figure 1** Principle of the atomic transient recorder. The initial time–momentum distribution of positive-energy (photo or Auger) electrons emitted from atoms excited by an attosecond pulse carries direct time-domain information about the excitation and relaxation dynamics of the electronic shell. A linearly polarized, few-cycle laser pulse, with its electric field directed parallel to the direction of observation of the ejected electrons, creates at different delays different tomographic projections of the time–momentum distribution  $n_e(p_i, t)$  of atomic electron emission on momentum space. These final momentum distributions can readily be measured after the laser pulse left the interaction region. In the absence of the laser field, the electron momenta do not change after detachment and accumulation of electrons with a given final momentum (mathematically: time-integration) follows lines of constant momentum (green lines) yielding the field-free final momentum distribution:  $\sigma_0(p) = \int_{-\infty}^{\infty} n_e(p, t) dt$  (green profile). In the presence of a probing field, accumulation of electrons with a given final momentum occurs along the lines of constant canonical momentum  $p_i + eA_L(t)$ , (blue and red lines, see equation (1)). The corresponding projections (streaked spectra) are represented in red and blue. From a suitable set of such tomographic projections the time–momentum distribution of electron emission can be retrieved, providing direct time-domain insight into atomic dynamics triggered by an attosecond excitation (in our experiments XUV pulse) synchronized to the probing laser field.

linearly polarized laser field  $E_L(t) = E_0(t)\cos(\omega_L t + \varphi)$  and observed within a narrow cone aligned parallel to the laser electric field vector is given by:

$$\sigma(p) = \int_{-\infty}^{\infty} n_e(p - eA_L(t), t) dt \quad (1)$$

where  $n_e(p_i, t)$  is the initial time–momentum distribution of emitted electrons and  $e$  is the electron charge. The vector potential in the Coulomb gauge  $A_L(t) = \int_t^{\infty} E_L(t') dt'$  accounts for the

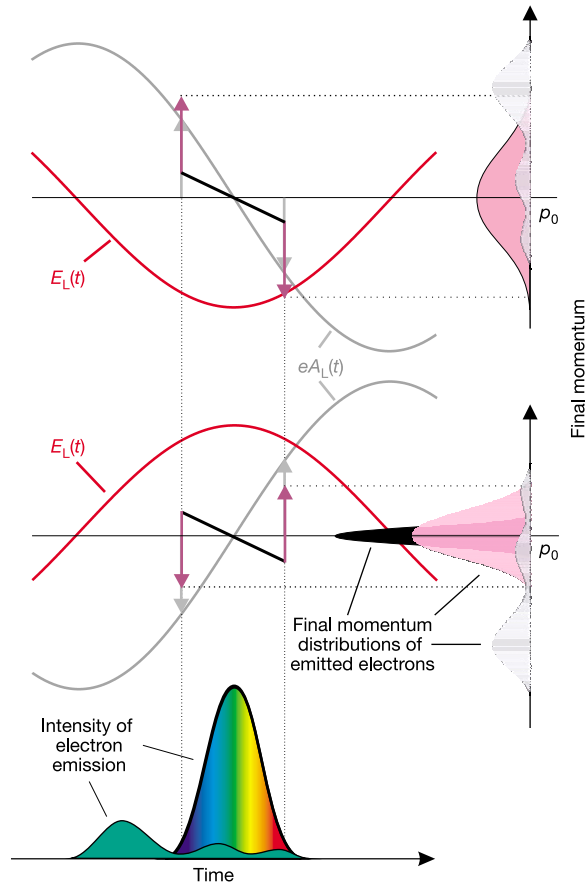


**Figure 2** Electron streak records in specific cases. The electric field vector of the linearly polarized probe laser pulse points towards the electron detector for  $E_L > 0$ . In the absence of a temporal sweep of initial momenta of the emitted atomic electrons, described by  $n_e(p_i, t) = f(p_i)g(t)$ , the momentum transfer  $\Delta p = eA_L(t_r)$  (grey line), maps the temporal emission profile  $g(t)$  (green profile) uniquely into a similar distribution of final momenta (grey profiles) around the mean initial momentum  $p_0$ , provided that the emission is temporally confined between adjacent zero transitions of the probing laser field  $E_L(t)$ . In this specific case, the temporal intensity profile of electron emission is directly mirrored by the streak record just as in a conventional streak camera. However, any sweep of the electrons' initial momentum (for example, a linear one as indicated by the black line for the single-peaked electron emission) revokes the unique correspondence between an electron's final momentum and its release time, preventing the retrieval of accurate temporal information from single streak records. In this case, at least two streak records (pink profiles)—in addition to the field-free spectrum (black profile)—are required. In the absence of a nonlinear temporal momentum sweep the streak records obtained near the zero transitions of  $A_L(t)$  with opposite slopes (pink profiles) together with the field-free spectrum (black profile) allow determination of all relevant characteristics: the temporal profile, duration and momentum chirp of emission. Note that a linear momentum sweep leads to an asymmetric broadening of the streaked spectra at these delays and it is this asymmetry that makes the measurement highly sensitive to the momentum sweep, that is, highly sensitive to deviations of the pulse duration from the Fourier limit.

momentum boost imparted to the free electron by the laser field from the time of its release  $t$  until the pulse has passed. In the classical description of the freed electrons' motion in the strong laser field, the final momentum spectrum can be viewed as a projection of  $n_e(p_i, t)$  along the lines where  $p = p_i + eA_L(t)$  is constant (see Fig. 1);  $p_i$  is the initial kinetic momentum of the electron. By delaying the laser emission, a set of tomographic records is obtained, from which the initial time–momentum distribution  $n_e(p_i, t)$  can be uniquely reconstructed if the emission terminates within  $T_0/2 = \pi/\omega_L$ . The method is closely related to frequency-resolved optical gating<sup>8,9</sup> with the oscillating laser field (rather than its envelope) being employed as a gate. In the simplest cases one or

two streaked spectra are sufficient for retrieving  $n_e(p_i, t)$ , as discussed in Fig. 2.

For our experiments the XUV excitation pulses have been generated from neon atoms ionized by an intense linearly polarized few-cycle laser pulse (full-width at intensity half-maximum (FWHM):  $\tau_L = 5$  fs, carrier wavelength:  $\lambda_L = 750$  nm,  $T_0 = 2.5$  fs) with controlled waveform<sup>5</sup> by a process that leads to the emission of high-order harmonics for multi-cycle drivers<sup>10,11</sup>. Proper adjustment of the laser peak intensity yielded highest-energy (cutoff) XUV emission in the high-reflectivity band of our Mo/Si multilayer mirror, which was used for focusing the XUV as well as laser pulses into another neon gas jet for recording atomic transients. Both an intuitive model<sup>12,13</sup> and extensive numerical simulations<sup>14–18</sup> predict the cutoff emission to be confined to the vicinity of zero transition(s) of the laser electric field after the most intense half-cycle(s) in a few-cycle driver.

Figure 3 summarizes representative streaked neon photoelectron spectra recorded with the XUV and laser pulse impinging with a fixed relative timing set in the XUV generation process. For a cosine driver waveform ( $\varphi = 0$ ), cutoff radiation (filtered by the Mo/Si multilayer) is predicted to be emitted in a single bunch at the zero transition of  $E_L(t)$  following the pulse peak. The photoelectrons knocked off in the direction of the peak electric field at this instant should gain the maximum increase of their momentum and energy. Figure 3d corroborates this prediction. The clear upshift is consistent with the XUV burst coinciding with the zero transition of the laser electric field (see Fig. 2). Possible satellites would appear at the adjacent zero transitions of  $E_L(t)$  and suffer an energy downshift. The absence of a downshifted spectral peak of substantial intensity indicates a clean single sub-fs pulse generation. With the phase

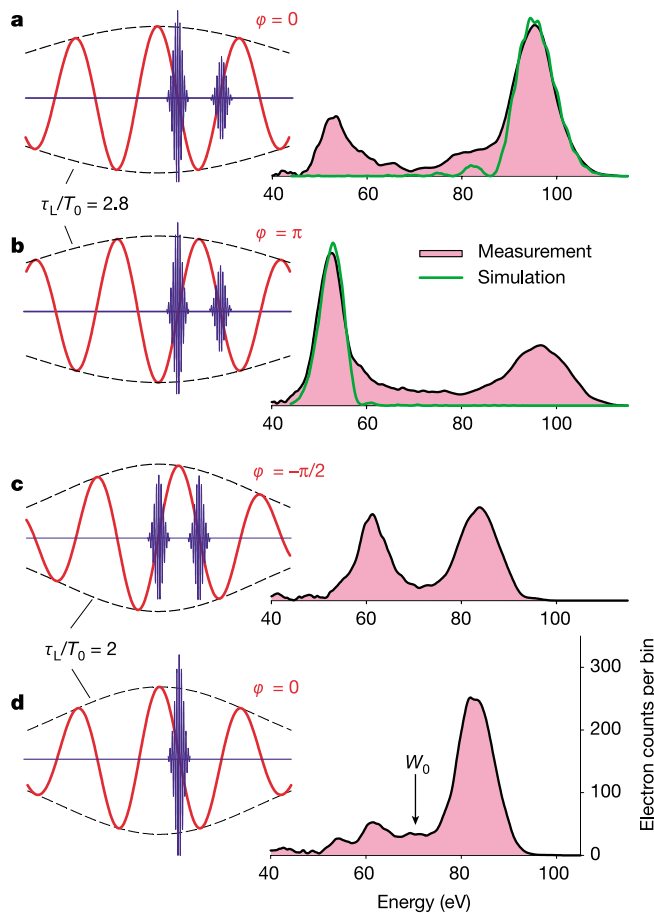


**Figure 3** Streaked photoelectron spectra recorded at a fixed delay of probe laser light. Energy distribution of photoelectrons emitted from neon atoms excited by a sub-fs XUV pulse carried at a photon energy of  $\hbar\omega_{\text{XUV}} \approx 93.5$  eV (selected by the Mo/Si mirror). The photoelectron spectrum peaks at  $W_0 = \hbar\omega_{\text{XUV}} - W_b \approx 72$  eV in the absence of  $E_L(t)$ , where  $W_b = 21.5$  eV is the binding energy of the most weakly bound valence electrons in Ne. The spectrally filtered cutoff XUV bursts and the 5-fs, 750-nm driver laser pulses are depicted by blue and red lines, respectively. **a, b**, Streaked spectra obtained with respectively ‘cosine’ and ‘-cosine’ laser pulses of a normalized duration of  $\tau_L/T_0 = 2.8$  and of a peak electric field of  $E_0 = 140$  MV cm<sup>-1</sup>. The green lines on the right-hand side depict spectra computed with an XUV burst derived from the measured asymmetric XUV radiation filtered by the mirror (see Fig. 5a) under the assumption of zero spectral phase. The satellite pulse is not modelled in this way, because the corresponding modulation of the spectrum was not considered in the calculation. The difference in broadening of the up- and down-shifted spectral features appears to be a consequence of the quadratic temporal frequency sweep resulting from the asymmetric spectral distribution of the XUV burst (see Fig. 5a). **c, d**, Streaked spectra obtained with respectively ‘sine’ and ‘cosine’ laser pulses characterized by  $\tau_L/T_0 = 2$  and  $E_0 = 75$  MV cm<sup>-1</sup>.

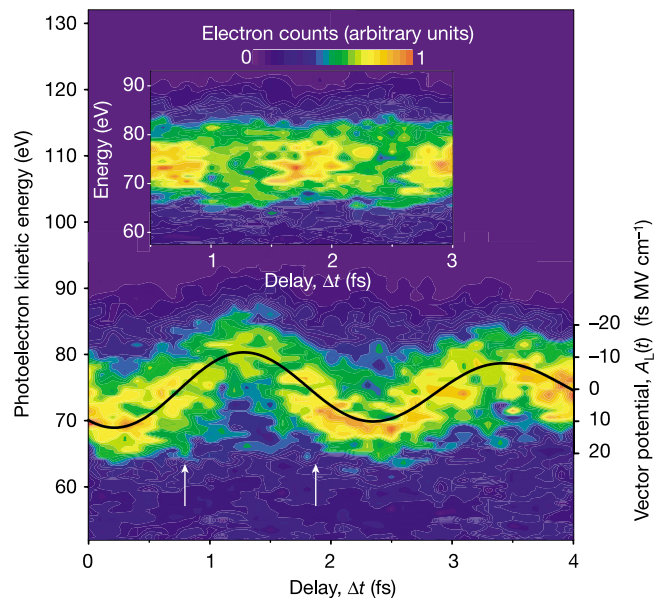


**Figure 4** ATR measurement: a series of tomographic projections (streaked kinetic energy spectra) of the initial time–momentum distribution of photoelectrons knocked out by a single sub-fs XUV pulse (in false-colour representation). A few-cycle laser pulse with a cosine waveform and a normalized duration of  $\tau_L/T_0 = 2$  was used for both generating the single 93-eV sub-fs excitation pulse and for probing photoelectron emission in the atomic transient recorder. Black line,  $A_L(t)$  of the probing field evaluated from the peak shift of the streaked spectra (see scale on the right hand side). From  $A_L(t)$  the electric field of the light wave can also be determined by using the relationship  $E_L(t) = -dA_L/dt$ . The electric field vector points towards the electron detector for  $E_L > 0$ . Inset, streaked spectra obtained under the same experimental conditions except for the carrier-envelope phase of the few-cycle pulse, which was left unstabilized.

adjusted to yield a sine waveform ( $\varphi = -\pi/2$ ), cutoff emission is predicted to come in twin pulses (Fig. 3c). The double-peaked streaked spectrum (Fig. 3c) clearly reflects this time structure. High-energy XUV photons are now distributed in two bursts, each of which is less than half as intense as the isolated burst produced by the cosine waveform (Fig. 3d). These measurements demonstrate how light waveform control allows shaping XUV emission on a sub-fs timescale.

Other than  $\varphi$  the normalized pulse duration  $\tau_L/T_0$  plays a crucial role in the generation of a single XUV pulse, as demonstrated by experiments with slightly longer, 7-fs laser pulses ( $\tau_L/T_0 = 2.8$ ). Under these conditions a satellite pulse is unavoidable for any setting of  $\varphi$  and most careful filtering of the cutoff photons (Fig. 3a, b). A reduced difference in intensity of the adjacent half-cycles of the few-cycle wave implies that the highest-energy spectral components of adjacent XUV bursts reach the energy band selected by our 15%-bandwidth bandpass filter.

With isolated sub-fs XUV pulses at our disposal atomic transients can now be triggered and their subsequent evolution be captured by probing electron emission with a synchronized wave of laser light in the atomic transient recorder (ATR). In the first ATR measurements presented here the objects of scrutiny were photoelectrons. Figure 4

shows a series of streaked spectra of photoelectrons emitted from neon at different delays of  $E_L(t)$ . If the electrons' initial kinetic energy is much larger than their average quiver energy, their laser-induced energy shift  $\Delta W(t) \approx (p_0/m)\Delta p(t) = (ep_0/m)A(t)$ , where  $m$  is the electron mass, probes  $A_L(t)$  directly at the instant  $t$  of electron release and allows its determination without having to analyse the structure of the streaked spectra. The evaluated  $A_L(t)$  is depicted by the black line in Fig. 4, revealing  $T_0/2 \approx 1$  fs at the pulse peak, which is indicative of a strong blue shift. This was observed previously and found to originate from ionization-induced self-phase modulation in the XUV source<sup>1</sup>. With  $A_L(t)$  known, we can set out to characterize the electron emission. Waveform control is as essential here as for the reproducible generation of sub-fs bursts (see Fig. 3); its absence smears the streak records beyond redemption (inset in Fig. 4).

Figure 5 depicts the photoelectron spectra in the absence of the probe laser field (Fig. 5a) and the streaked spectra (Fig. 5b, c) recorded at adjacent zero transitions of  $A_L(t)$ , which are most sensitive to a possible quadratic spectral phase (linear chirp) carried by the XUV pulse. The best fits to these data (blue lines in Fig. 5) yield  $\tau_{\text{XUV}} = 250(-5/+30)$  as and  $\tau_{\text{jitter}} = 260(\pm 80)$  as for the duration and jitter of the XUV pulse, respectively. The remarkable accuracy of  $\tau_{\text{XUV}}$  derives from the use of several tomographic projections of the time-momentum distribution of photoelectrons (spectra shown in Fig. 5). The inspection of other streaked spectra justified the neglect of higher-order spectral phase in the above analysis. The large jitter appears to be extrinsic (vibrations due to the vacuum pumps) because it is virtually absent in the absence of a delay between XUV and laser pulse (Fig. 3). The temporal intensity profile and chirp of the XUV pulse obtained from the ATR measurements are shown in Fig. 5d. The pulse is Fourier-limited with a weak temporal chirp resulting from the asymmetric shape of the pulse spectrum (Fig. 5a).

The briefest time interval within which two different atomic events can be recognized as different by our apparatus is ultimately limited by quantum mechanical uncertainty. This dictates that any short time structure comes with a broad energy spectrum. In order that the streaks of two events separated by  $\delta t$  in time can be resolved they must be shifted with respect to each other by at least as much as their own spectral width  $\delta W \approx \hbar/\delta t$ . From this requirement we obtain the ATR resolving power as:

$$\delta t = \frac{T_0}{2\pi} \sqrt{\frac{\hbar\omega_L}{\Delta W_{\text{max}}}} \quad (2)$$

where  $\Delta W_{\text{max}}$  stands for the energy shift suffered by the electron ejected at the peak of  $A_L(t)$ . Under our current experimental conditions  $\Delta W_{\text{max}}$  can approach 25 eV before the onset of laser-induced ionization, yielding  $\delta t < 100$  as for  $T_0 = 2$  fs. The atomic transient recorder driven by red light and probing electrons with a kinetic energy near 100 eV is able to distinguish events within 100 as, constituting what is to our knowledge the shortest interval of time directly measurable to date.

Extension of the presented experiments to simultaneously exploring the temporal variation of emission intensity and momentum distribution of primary (photo) and secondary (Auger) electron emission will provide unprecedented insight into the excitation and relaxation dynamics of the electronic shell of atoms and molecules. The currently used time window of  $T_0/2 \approx 1$  fs can be extended to several 10 fs by difference frequency generation with the few-cycle laser pulse while keeping the resolution of the ATR in the sub-fs regime, owing to  $\delta t \propto \sqrt{T_0}$ . With an extended time window a detailed characterization of trains of attosecond bursts (in contrast with the measurement of parameters averaged over the train<sup>19-21</sup>) will also become feasible. At near-keV excitation energies, the atomic transient recorder will allow time-domain metrology with a resolution approaching the atomic unit of time (24 as). □

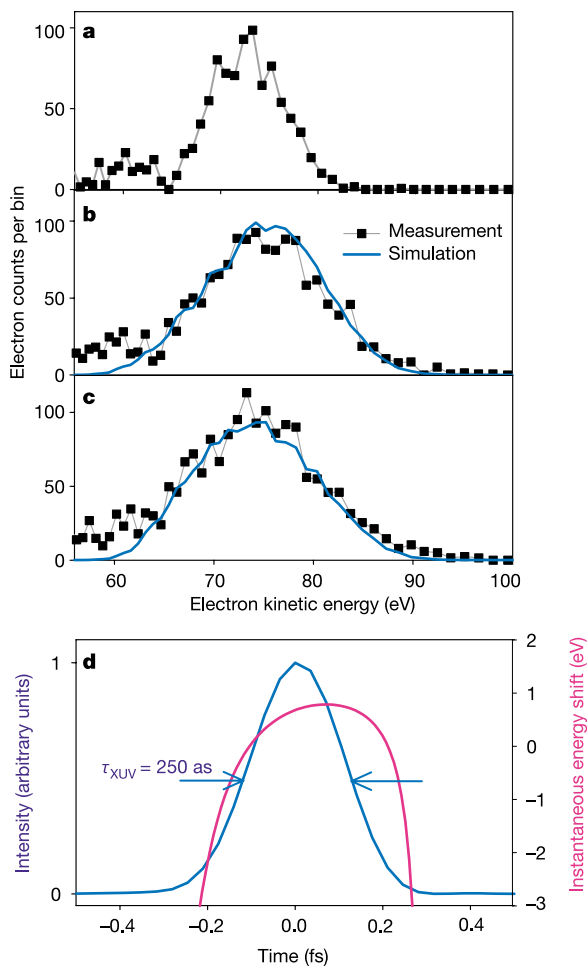


**Figure 5** Selected streaked spectra from the ATR measurement of photoelectron emission from neon excited with a 93-eV sub-fs pulse (Fig. 4). **a**, Spectrum in the absence of laser field. **b**, **c**, Streaked spectra recorded at delays that imply coincidence of electron emission with (adjacent) zero transitions of  $A_L(t)$ , see arrows in Fig. 4. **d**, Temporal intensity profile and energy sweep of the sub-femtosecond XUV excitation pulse evaluated from the ATR measurements.

Methods

We sample electron emission from atoms using the experimental set-up that was described in detail<sup>1</sup> and employed recently for probing Auger electrons on a few-fs timescale<sup>22</sup>. The essential innovation here is that waveform-controlled few-cycle light now provides a reproducible excitation burst for accurate triggering and a reproducible streaking field for capturing sub-fs electron emission from atoms. For excitation, XUV bursts are produced from Ne atoms ionized by intense, few-cycle waveform-controlled light pulses<sup>5</sup> in a process giving rise to high-order harmonics of the incident light for periodic (multi-cycle) pumping<sup>10,11</sup>. The collinear XUV and laser beams are focused into a neon gas jet and delayed with respect to each other for the ATR measurements with a two-component Mo/Si broadband multilayer mirror<sup>1</sup> (radius of curvature = -70 mm) placed 2.5 m downstream from the source. The internal part of the laser beam (~3 mm in diameter) was blocked with a zirconium filter (transmitting the XUV pulse) in front of the Mo/Si mirror. The resultant annular laser beam (with a dark spot 3 mm in diameter in its centre) and the XUV beam (~3 mm in diameter) confined by the annular laser beam were focused by the external and internal sections of the two-component Mo/Si mirror<sup>1</sup>, respectively. The two components can be aligned separately and translated with respect to each other along the optical axis of the mirror.

The reflectivity band of the multilayer extends from 85 V to 100 V with a peak reflectance of ~30% and a FWHM of ~9 V. Electrons ejected following the XUV excitation are collected within a narrow cone (<4°) aligned parallel to the laser and XUV polarization and analysed with a time-of-flight spectrometer. Two types of experiments have been implemented. First, by removing the zirconium filter we used the internal part of the Mo/Si mirror to focus both the XUV and the laser beam to eliminate any external source of fluctuations in the timing between the excitation and probing pulses (results summarized in Fig. 3). In the second type of studies, the XUV and the laser beam were reflected by different sections of the focusing mirror as described above. In these investigations the probing laser field could be delayed with respect to the XUV excitation pulse by the translation of the internal part of the mirror on a nanometre scale, yielding the data shown in Figs 4 and 5.

Received 24 October; accepted 5 December 2003; doi:10.1038/nature02277.

1. Hentschel, M. *et al.* Attosecond metrology. *Nature* **414**, 509–513 (2001).
2. Zewail, A. Femtochemistry: atomic-scale dynamics of the chemical bond (adapted from the Nobel Lecture). *J. Phys. Chem. A* **104**, 5660–5694 (2000).
3. Itatani, J. *et al.* Attosecond streak camera. *Phys. Rev. Lett.* **88**, 173903 (2002).
4. Kitzler, M., Milosevic, N., Scrinzi, A., Krausz, F. & Brabec, T. Quantum theory of attosecond XUV pulse measurement by laser-dressed photoionization. *Phys. Rev. Lett.* **88**, 173904 (2002).
5. Baltuska, A. *et al.* Attosecond control of electronic processes by intense light fields. *Nature* **421**, 611–615 (2003).
6. Bradley, D. J., Liddy, B. & Sleat, W. E. Direct linear measurement of ultrashort light pulses with a picosecond streak camera. *Opt. Commun.* **2**, 391 (1971).
7. Schelev, M. Ya., Richardson, M. C. & Alcock, A. J. Image-converter streak camera with picosecond resolution. *Appl. Phys. Lett.* **18**, 354 (1971).
8. Kane, D. J. & Trebino, R. Characterization of arbitrary femtosecond pulses using frequency-resolved optical gating. *IEEE J. Quantum Electron.* **29**, 571–579 (1993).
9. Sekikawa, T., Katsura, T., Miura, S. & Watanabe, S. Measurement of the intensity-dependent atomic dipole phase of a high harmonic by frequency-resolved optical gating. *Phys. Rev. Lett.* **88**, 193902 (2002).
10. L'Huillier, A. & Balcou, Ph. High-order harmonic generation in rare gases with a 1-ps 1053-nm laser. *Phys. Rev. Lett.* **70**, 774–777 (1993).
11. Macklin, J. J., Kmetec, J. D. & Gordon, C. L. III High-order harmonic generation using intense femtosecond pulses. *Phys. Rev. Lett.* **70**, 766–769 (1993).
12. Schafer, K. J., Yang, B., DiMauro, L. F. & Kulander, K. C. Above threshold ionization beyond the high harmonic cutoff. *Phys. Rev. Lett.* **70**, 1599–1602 (1993).
13. Corkum, P. B. Plasma perspective on strong-field multiphoton ionization. *Phys. Rev. Lett.* **71**, 1994–1997 (1993).
14. Lewenstein, M., Balcou, Ph., Ivanov, M. Yu., L'Huillier, A. & Corkum, P. B. Theory of high-harmonic generation by low-frequency laser fields. *Phys. Rev. A* **49**, 2117–2132 (1994).
15. Christov, I. P., Murnane, M. M. & Kapteyn, H. C. High-harmonic generation of attosecond pulses in the “single-cycle” regime. *Phys. Rev. Lett.* **78**, 1251–1254 (1997).
16. Kan, C., Burnett, N. H., Capjack, C. E. & Rankin, R. Coherent XUV generation from gases ionized by several cycle optical pulses. *Phys. Rev. Lett.* **79**, 2971–2974 (1997).
17. de Bohan, A., Antoine, P., Milosevic, D. B. & Piraux, B. Phase-dependent harmonic emission with ultrashort laser pulses. *Phys. Rev. Lett.* **81**, 1837–1840 (1998).
18. Tempea, G., Geissler, M. & Brabec, T. Phase sensitivity of high-order harmonic generation with few-cycle laser pulses. *J. Opt. Soc. Am. B* **16**, 669–674 (1999).
19. Paul, P. M. *et al.* Observation of a train of attosecond pulses from high harmonic generation. *Science* **292**, 1689–1692 (2001).
20. Mairesse, Y. *et al.* Attosecond synchronisation of high-harmonic soft X-rays. *Science* **302**, 1540–1543 (2003).
21. Tzallas, P., Charalambidis, D., Papadogiannis, N. A., Witte, K. & Tsakiris, G. D. Direct observation of attosecond light bunching. *Nature* **426**, 267–271 (2003).
22. Drescher, M. *et al.* Time-resolved atomic inner-shell spectroscopy. *Nature* **419**, 803–807 (2002).

**Acknowledgements** This work was sponsored by the Fonds zur Förderung der wissenschaftlichen Forschung (Austria), the Deutsche Forschungsgemeinschaft and the Volkswagenstiftung (Germany) and by the European Union's Human Potential Programme.

**Competing interests statement** The authors declare that they have no competing financial interests.

**Correspondence** and requests for materials should be addressed to F.K. (ferenc.krausz@tuwien.ac.at).

Giant magnetoresistance in organic spin-valves

Z. H. Xiong, Di Wu, Z. Valy Vardeny & Jing Shi

Department of Physics, University of Utah, Salt Lake City, Utah 84112, USA

A spin valve is a layered structure of magnetic and non-magnetic (spacer) materials whose electrical resistance depends on the spin state of electrons passing through the device and so can be controlled by an external magnetic field. The discoveries of giant magnetoresistance<sup>1</sup> and tunnelling magnetoresistance<sup>2</sup> in metallic spin valves have revolutionized applications such as magnetic recording and memory, and launched the new field of spin electronics<sup>3</sup>—‘spintronics’. Intense research efforts are now devoted to extending these spin-dependent effects to semiconductor materials. But while there have been noteworthy advances in spin injection and detection using inorganic semiconductors<sup>4–6</sup>, spin-valve devices with semiconducting spacers have not yet been demonstrated.  $\pi$ -conjugated organic semiconductors may offer a promising alternative approach to semiconductor spintronics, by virtue of their relatively strong electron-phonon coupling<sup>7</sup> and large spin coherence<sup>8</sup>. Here we report the injection, transport and detection of spin-polarized carriers using an organic semiconductor as the spacer layer in a spin-valve structure, yielding low-temperature giant magnetoresistance effects as large as 40 per cent.

$\pi$ -conjugated organic semiconductors (OSEs) are a relatively new class of electronic materials that are revolutionizing important technological applications including information display<sup>9</sup> (ref. 10 and references therein) and large-area electronics (ref. 11 and references therein), owing to their ability to be economically processed in large areas, their compatibility with low-temperature processing, the tunability of their electronic properties, and the simplicity of thin-film device fabrication. The virtually limitless flexibility of synthetic organic chemistry allows the fabrication of  $\pi$ -conjugated OSE structures with a degree of control unattainable with the conventional inorganic semiconductors. In addition, the OSEs have extremely weak spin-orbit interaction and weak hyperfine interaction, so that electron spin diffusion length is especially long<sup>8</sup>. These properties make them ideal for spin-polarized electron injection and transport applications.

Here we have chosen the small  $\pi$ -conjugated molecule 8-hydroxy-quinoline aluminium (Alq<sub>3</sub>), most commonly used in organic light-emitting diodes (OLEDs)<sup>10</sup>, to serve as an OSE spacer in organic spin-valves, because it can easily be deposited as thin films and integrated with a variety of metallic electrodes. As shown in Fig. 1a, the vertical organic spin-valves that we fabricated consist of three layers: two ferromagnetic electrode films (FM<sub>1</sub> and FM<sub>2</sub>, respectively) and the OSE spacer. By engineering the two FM electrodes to have different coercive fields ( $H_{c1}$  and  $H_{c2}$ , respectively), their magnetization directions can have either a parallel or anti-parallel alignment configuration when sweeping the external magnetic field,  $H$ ; this is essential for proving the spin-valve effect.

Intrigued by the possibility of spin-injection involving a  $\pi$ -conjugated OSE oligomer (sexi-thiophene, T<sub>6</sub>)<sup>12</sup>, where both the opposite FM electrodes were La<sub>0.67</sub>Sr<sub>0.33</sub>MnO<sub>3</sub> (LSMO), we have chosen LSMO for the bottom electrode (FM<sub>1</sub>) and cobalt as the top electrode (FM<sub>2</sub>) in our devices (Fig. 1a, b). LSMO is believed to be a half-metallic ferromagnet that possesses near-100% spin-polarization<sup>13</sup>. We note that unlike metallic FM films such as cobalt, nickel, iron or their alloys, the LSMO films are already stable against oxidation. In fact, our LSMO films have been cleaned and re-used